

Supplementary Material: A Diffeomorphic Vector Field Approach to Analyze the Thickness of the Hippocampus from 7T MRI

I. HIPPOCAMPAL SUBREGIONS MANUAL SEGMENTATION PROTOCOL

This appendix describes the protocol that we devised and used to segment the subregions of the hippocampus. The protocol was first designed on post-mortem T2-weighted images and subsequently adapted in order to handle in-vivo T2-weighted images. It extends the previous protocol presented in [1] and [2] through several aspects: i) boundary definition using post-mortem ultra-high-resolution MRI and subsequent adaptation to in-vivo 7T MRI; ii) reduced number of arbitrary landmarks; iii) segmentation over the full length of the hippocampus and not only the hippocampal body.

In order to design the protocol, we used post-mortem data acquired at 9.4T ($0.3 \times 0.2 \times 0.2$ mm resolution) by the University of Pennsylvania [3] and used in Section III-A of the present paper as well as in-vivo data acquired at Neurospin (CEA Saclay, France, see [4]) on a 7T Siemens MRI scanner ($0.3 \times 0.3 \times 1.2$ mm resolution) with a Nova Medical 32 receiving channel coil, perpendicular to the hippocampal main axis.

Anatomical boundaries are defined based on [5] and [6] as well as on in-house histological sections. In both in-vivo and ex-vivo data we identify the uncus (the most medial part of the temporal lobe). Referring to its position, we isolate three subparts of the hippocampus (body, head and tail) for which the following structures (see Fig. 1) are delineated: 1) alveus; 2) SRLM assumed to correspond to the strata radiatum, lacunosum and moleculare of CA1-3 and the strata lacunosum and moleculare of the subiculum (i.e. the layers poorer in neuronal bodies); 3) hilum corresponding to the stratum pyramidale of CA4 and the stratum granulosum and polymorphic layer of DG, which are the layers richer in neuronal bodies; 4) Cornu Ammonis Stratum Pyramidale (CA-SP), assumed to correspond to the stratum pyramidale of CA1-3, the layer richer in neuronal bodies of CA1-3; 5) subiculum-SP corresponding to the stratum pyramidale of the subiculum, layer richer in neuronal bodies of the subiculum; 6) fimbria. The structures are segmented in the coronal plane, slice by slice, following a specific order whenever possible (alveus, SRLM, hilum, CA-SP, subiculum, fimbria), with references to sagittal and axial planes to ensure 3D consistency. Specific definitions are considered for the hippocampal body, head and tail, as the shape of the digitationes hippocampi and the change of orientation in head and tail make segmenting those a much more complex task.

The manual segmentation protocol consists of two steps: the limits of the head, body and tail of the hippocampus are first

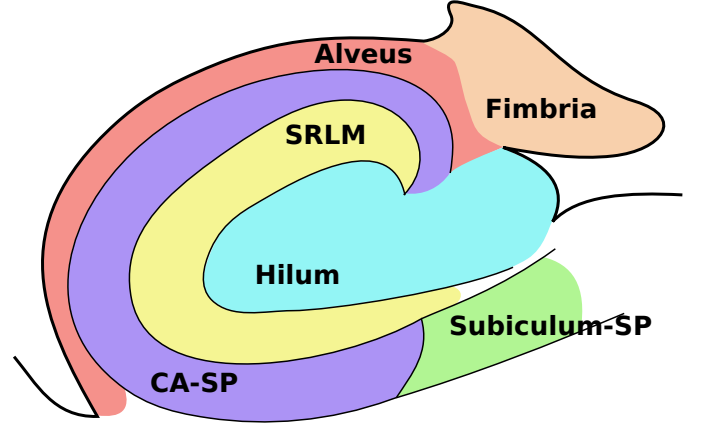


Fig. 1: Map (coronal view, adapted from [5]) of the hippocampal subregions the segmentation protocol delimits: Alveus; SRLM: strata radiatum, lacunosum and moleculare of CA1-3 and strata lacunosum and moleculare of the subiculum; Hilum: stratum pyramidale of CA4 and stratum granulosum plus polymorphic layer of DG; CA-SP: stratum pyramidale of CA1-3; Subiculum-SP: stratum pyramidale of the subiculum; fimbria.

identified, and next the subregions are delineated according to our predefined labels (first in the body, then in the head and finally in the tail).

A. Head, body and tail identification

The most anterior slice of the hippocampal body is the easiest to delimit: when scrolling from front to back, it corresponds to the first slice where the median part of the hippocampus (the uncus) is no longer visible (Fig. 2a in red). To identify the most posterior slice of the body, we follow a geometric feature: the change in orientation of the main hippocampal axis (Fig. 2b in red), after which the cornu Ammonis and the gyrus dentatus begin to lose their usual C-shaped configuration in coronal planes, whereas the fimbria enlarges and acquires a “fan” shape at the superior-medial border of the hippocampus. Both the most anterior and posterior body limits are confirmed in the sagittal plane.

The most anterior limit of the hippocampus is the beginning of its head, which is easily identifiable. Since the head is anteriorly covered by the alveus, the first head slice is marked by the appearance of gray matter “inside” white matter (Fig. 2c in red).

Finally, the most posterior limit of the hippocampus, the end of its tail, is the hardest to define. It is detected by checking the appearance of a usual sulcus shape. Indeed, in the anterior part of the tail, the cornu Ammonis has a configuration similar

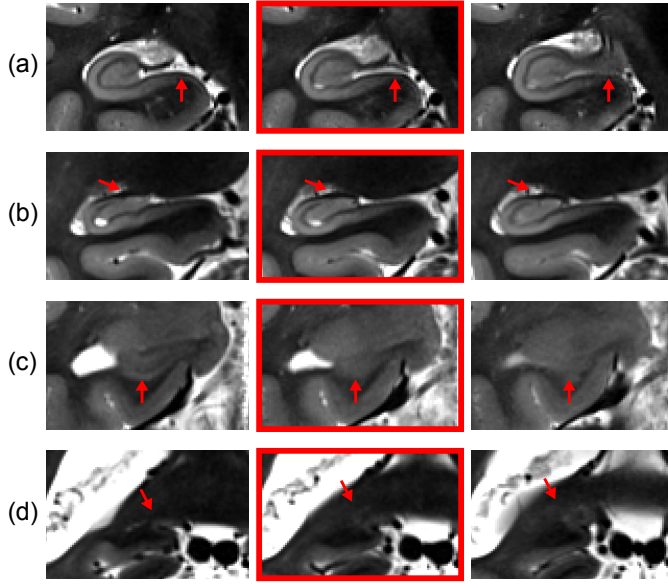


Fig. 2: Identification of: (a) the most anterior slice of the body; (b) the most posterior limit of the body; (c) the anterior limit of the hippocampus; (d) the posterior limit of the hippocampus. The chosen delimiting slices are highlighted in red.

to that of the body. Progressively, the cornu Ammonis presents folds of decreasing size, whereas small protrusions of the gyrus dentatus are still visible. Then, in the posterior part of the tail, the cornu Ammonis becomes smooth and narrow, until it takes the shape of a “classical” gyrus (Fig. 2d in red).

B. Segmentation of hippocampal subregions

After the anteroposterior limits of the three main segments (head, body and tail) have been identified, the subregions are delineated within each segment separately. First, the hippocampal body is segmented, from the most anterior to the most posterior slice. Next, the head is segmented from the most posterior to the most anterior slice, since it is easier to segment the posterior part of the head by taking into account the delineation of the body. To conclude, we segment the tail from the most anterior to the most posterior slice. At all stages, references are made to sagittal and axial planes to ensure 3D consistency.

1) *Segmentation in the hippocampal body*: Subregions of the hippocampal body, see Fig. 3a, are segmented in the following order.

a) *Alveus*: The inferior border is defined at the junction between the collateral eminence and the alveus when the temporal horn is not collapsed. Its superior border is defined as the point where the alveus enters the hilum.

b) *SRLM*: The SRLM is located between the hippocampal ribbon (CA-SP/Subiculum-SP) and the hilum (when it is present) or as the darker band above the hippocampal ribbon when the hilum is not in front of the ribbon. Its inferior-medial end corresponds to the most medial part of the subiculum, whereas its superior end is clearly visible when CA goes into the hilum. Its other borders are well defined by the signal. In some cases, the vestigial sulcus is dilated and becomes clearly visible; it is not included in the SRLM.

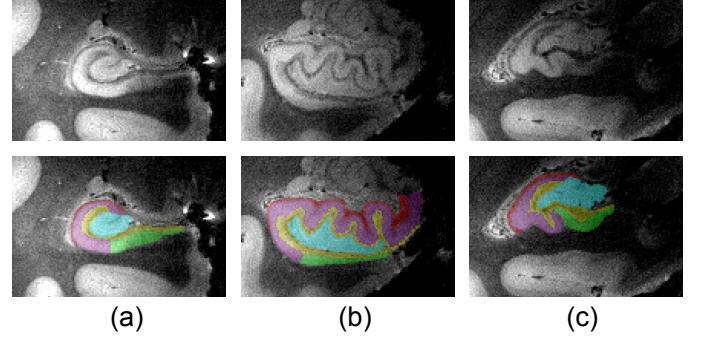


Fig. 3: Top: coronal slices of the hippocampal (a) body, (b) head and (c) tail. Bottom: corresponding manual segmentations. Red - alveus, purple - CA-SP, green - subiculum, yellow - SRLM, light blue - hilum.

c) *Hilum*: Its borders are mostly defined by that of the SRLM, except for its superior and medial limits. The superior limit corresponds to the boundary with CA and does not match a signal contrast. It is therefore defined by tracing an imaginary line between the superior ends of SRLM and alveus. The medial limit with the cerebrospinal fluid (CSF) is defined by a signal change.

d) *CA-SP*: Most of its limits are defined as its boundaries with the alveus, the SRLM and the hilum. The only border that remains to be determined is its inferior boundary with the subiculum. This is defined in a purely geometric manner to correspond to the middle of the hilum so as to mimic the ratio observed in anatomical atlases.

e) *Subiculum*: The lateral border is given by CA-SP, whereas the superior and inferior borders are given respectively by the SRLM and the white matter of the parahippocampal gyrus. The medial limit is arbitrary as there is no clear contrast change between the subiculum and adjacent cortices. It is defined as the inflexion point of the superior part of the parahippocampal gyrus, as it corresponds also to a thinning of the structure.

f) *Fimbria*: It is considered as the round shaped prolongation of the alveus when it separates from CA-SP. Due to image artefacts it is practically impossible to reliably define it on post-mortem data.

2) *Segmentation in the hippocampal head*: See Fig. 3b for an illustration of the segmentation in the hippocampal head. Segmenting the structures relies on an earlier delineation of the uncus and is done in the same order as for the hippocampal body, with the exception of the CA-SP which does not require prior segmentation of the hilum (that is not visible in all slices in the head) and is delineated before it.

a) *Alveus*: The superior border differs from that found in the hippocampal body, for the most anterior slices of the head. In the most anterior slices, the hippocampus is folded on itself and the limit of the alveus is defined as the most medial point of the dark signal band covering the hippocampus. For the other slices, limits are mostly defined as in the hippocampal body.

b) *SRLM*: For the most anterior slices or the most medial parts of posterior slices, the SRLM lies between CA-SP and the subiculum or between separate parts of CA-SP. There, its

position is determined in the sagittal and axial planes to ensure 3D consistency. Outside those areas, it is located between the hippocampal ribbon and the hilum, as in the hippocampal body.

c) *CA-SP*: In the slices where SRLM cannot be clearly delineated, CA-SP is defined as the gray matter below the alveus. In all other slices, SRLM borders with CA-SP. The limit between CA-SP and the subiculum is arbitrarily defined and based on the curvature of SRLM to mimic what is reported in the atlases. In the amygdalo-hippocampal transition area, the superior border with the alveus is geometrically defined. After the posterior part of the uncus separates into its medial part, the segmentation of CA-SP follows the same rules as in the body. When the posterior part of the uncus separates from the ribbon, the subregions within the uncus cannot be easily discriminated and are treated as “uncus” as a whole. In this area, the segmentation of the remainder of CA-SP follows the same rules as in the body.

d) *Hilum*: Its borders with SRLM are defined by a signal change. Due to the complex shape of hippocampal digitations it can embed several connected components in coronal slices.

e) *Subiculum*: The lateral border is defined by CA-SP, whereas the medial border is the same as in the hippocampal body.

3) *Segmentation in the hippocampal tail*: See Fig. 3c for an illustration of the segmentation in the hippocampal tail. Subregions are segmented in approximately the same order as the one followed for the hippocampal body.

a) *Alveus*: The inferior border is defined as in the body. Its superior border is characterized by a thickening of the “fan-shaped” white matter lamina.

b) *SRLM*: It is located between CA-SP and the hilum. Its boundaries follow the same definitions as in the body. The basic frame of the subregions may be identified more easily on sagittal and axial planes, the precise delineation being done in the coronal plane. When no hilum is visible, the same rules as in the anterior part of the head apply.

c) *Hilum*: Its boundaries are defined as a signal change with respect to SRLM. When the body-like organization is no longer visible, the arbitrary limit with CA-SP is defined by the imaginary line between the end of SRLM and the basis of the fan-like white matter superior to the alveus, while ensuring 3D consistency.

d) *CA-SP*: It is defined as the part of the hippocampal ribbon that prolongs CA-SP of the body. Regarding the limits of CA-SP and the subiculum, in the most posterior slices with sulcus-like aspect, only CA-SP is visible. The transition between the body-like aspect and the sulcus-like aspect is to be confirmed on sagittal and axial planes, to ensure 3D consistency.

e) *Subiculum*: It prolongs the part of the subiculum defined in the body and gradually disappears towards the sulcus-like aspect. The medial part follows the same definition as in the body.

C. Inter-rater variability

Oblique coronal 2D T2-weighted fast spin-echo MR images were acquired on a Siemens 7T MRI scanner (Erlangen,

Germany), using a 32-channel head coil, for a set of 7T MRI of four control subjects (two men and two women, with a mean age of 36 years). Each image corresponds to a volume composed of 1.2mm-thick slices with 0.3mm×0.3mm in-plane resolution. For each image, two expert raters (authors J. Germain and L. Marrakchi-Kacem) manually segmented hippocampal subregions across the whole hippocampus following the protocol described in this appendix.

In order to assess the inter-rater variability of our segmentation protocol, mean inter-rater Dice coefficients averaged across the four subjects were computed (along with their standard deviation) for all subregions of the left and right hippocampi. These are reported in table I and table II respectively.

II. ELEMENTS OF HILBERT SPACE THEORY

A vector space H over \mathbb{R} is a Hilbert space if: H has a norm induced by an inner product between any two vectors h and h' in H , denoted $(h, h') \rightarrow \langle h, h' \rangle_H$, and the associated norm is $\|h\|_H^2 = \langle h, h \rangle_H$; H is a complete space for the topology associated to the norm. A Hilbert space isometry between two Hilbert spaces H and H' is an invertible linear map $F : H \rightarrow H'$ such that, for all $h, h' \in H \times H$, $\langle Fh, Fh' \rangle_{H'} = \langle h, h' \rangle_H$.

If H only meets the first condition, it is called a pre-Hilbert space, in which the Schwartz inequality holds: $\forall h, h' \in H \times H$, $\langle h, h' \rangle_H \leq \|h\|_H \|h'\|_H$.

The dual space of a normed vector space H , denoted by H^* is the space containing all continuous linear functionals $\Phi : H \rightarrow \mathbb{R}$. We adopt the notation $\Phi(h) = (\Phi, h)$ for $\Phi \in H^*$ and $h \in H$. H being a normed space, H^* also has a normed space structure, defined by: $\|\Phi\|_{H^*} = \max\{(\Phi, h) : h \in H, \|h\|_H = 1\}$.

Let H be a Hilbert space. For all $h \in H$, the function $\Phi_h : h' \rightarrow \langle h, h' \rangle_H$ belongs to H^* , and by the Schwartz inequality we have $\|\Phi_h\|_{H^*} = \|h\|_H$. A Hilbert space H may be identified with its dual H^* by the Riesz representation theorem, which states that, if $\Phi \in H^*$, there exists a unique $h \in H$ such that $\Phi = \Phi_h$. With a slight abuse of notation, we will identify h and Φ_h .

a) *Reproducing Kernel Hilbert Space (RKHS)*: Intuitively, an RKHS is a Hilbert space that uses a kernel representation to describe a problem in a high-dimensional feature space through continuous linear functionals. Its main properties are listed below. Let V be a Hilbert space embedded in the space of continuous functions $C^0(\Omega, \mathbb{R}^d)$. Consider $\Omega \subset \mathbb{R}^d$ and take $x \in \Omega$. The linear function δ_x defined by $(\delta_x, v) = v(x)$ is called the evaluation function. If δ_x is continuous on V , then V is called a Reproducing Kernel Hilbert Space (RKHS). For all $\alpha \in \mathbb{R}^d$, we will denote by $\alpha \otimes \delta_x$ the linear form such that $(\alpha \otimes \delta_x, v) = \alpha^T v(x)$. By the Riesz theorem, there exists an element $K_x^\alpha \in V$ such that, for any $v \in V$, $\langle K_x^\alpha, v \rangle_V = \alpha^T v(x)$.

The map $\alpha \Rightarrow K_x^\alpha$ is linear from \mathbb{R}^d to V , which implies that, for $y \in \Omega$, the map $\alpha \Rightarrow K_x^\alpha(y)$ is linear from \mathbb{R}^d to \mathbb{R}^d . We will denote by $K(y, x)$ the matrix such that, for $\alpha \in \mathbb{R}^d, x, y \in \Omega$, $K_x^\alpha(y) = K(y, x)\alpha$. This function K is called the reproducing kernel of V , and has several interesting properties, such as the self-reproducing property:

Segment	CA-SP	subiculum	SRLM	alveus	hilum	fimbria
Head	0.82(0.01)	0.75(0.02)	0.75(0.03)	0.76(0.03)	0.88(0.02)	N/A
Body	0.86(0.05)	0.87(0.04)	0.82(0.02)	0.79(0.05)	0.92(0.01)	0.72(0.04)
Tail	0.76(0.05)	0.70(0.08)	0.76(0.05)	0.50(0.16)	0.70(0.17)	N/A
All	0.81(0.02)	0.82(0.04)	0.78(0.01)	0.74(0.04)	0.89(0.02)	0.70(0.04)

TABLE I: Left hippocampus: average inter-rater Dice coefficients for manually segmented subregions of the hippocampus. Results are given for the head, body and tail of the hippocampus, as well as for its whole extent, and are presented as *mean(std)*. N/A is indicative of segments where a structure has not been segmented.

Segment	CA-SP	subiculum	SRLM	alveus	hilum	fimbria
Head	0.84(0.02)	0.78(0.04)	0.76(0.01)	0.75(0.03)	0.86(0.05)	N/A
Body	0.87(0.01)	0.88(0.01)	0.83(0.01)	0.74(0.08)	0.92(0.01)	0.72(0.14)
Tail	0.78(0.05)	0.85(0.06)	0.70(0.07)	0.46(0.26)	0.87(0.02)	N/A
All	0.83(0.01)	0.84(0.01)	0.78(0.01)	0.73(0.05)	0.89(0.02)	0.72(0.14)

TABLE II: Right hippocampus: average inter-rater Dice coefficients for manually segmented subregions of the hippocampus. Results are given for the head, body and tail of the hippocampus, as well as for its whole extent, and are presented as *mean(std)*. N/A is indicative of segments where a structure has not been segmented.

$\forall x, y \in \Omega, \alpha, \beta \in \mathbb{R}^d, \langle K(\cdot, x)\alpha, K(\cdot, y)\beta \rangle_V = \alpha_T K_y \beta(x) = \alpha_T K(x, y)\beta$. By the symmetric property of the inner product, we obtain : $K(y, x) = K(x, y)^T$. K is also positive definite, in the sense that, for any family $x_1, \dots, x_d \in \Omega$ and any $\alpha_1, \dots, \alpha_d$:

$$\sum_{i,j=1}^d \alpha_i \alpha_j K(x_i, x_j) \geq 0 \quad \sum_{i,j=1}^d \alpha_i \alpha_j K(x_i, x_j) = 0 \quad (1)$$

$$\Leftrightarrow \alpha_1 = \dots = \alpha_d = 0$$

Finally, for any $v \in V^*$, we have $\|v\|_{V^*}^2 = \int_{\Omega} v(x)^T K(x, y) v(y) dx dy$.

III. PROOFS OF RESULTS

A summary of the mathematical formulation presented in Section II of the present paper is given below, as well as the proofs to theorems enunciated in the same section.

1) *Isotropic images*: Let $\Omega \subset \mathbb{R}^d$ ($d = 2$ or $d = 3$) be a domain representing a hippocampal ribbon, $\partial\Omega$ its boundary, and n the outward normal to $\partial\Omega$. The boundary $\partial\Omega$ is further decomposed into its inner ($\partial\Omega_i$), outer ($\partial\Omega_o$) and “wall” ($\partial\Omega_w$) parts, such that $\partial\Omega = \partial\Omega_i \cup \partial\Omega_o \cup \partial\Omega_w$. Let v be a smooth vector field v running from $\partial\Omega_i$ to $\partial\Omega_o$. Consider $x \in \partial\Omega$ and let $\epsilon : \partial\Omega \rightarrow \{-1; 0, 1\}$ be a function defining the orientation of the normal vector in $\partial\Omega$ such that:

$$\epsilon(x) = \begin{cases} -1 & , \text{ if } x \in \partial\Omega_i \quad (\text{inward orientation}) \\ 0 & , \text{ if } x \in \partial\Omega_w \\ 1 & , \text{ if } x \in \partial\Omega_o \quad (\text{outward orientation}) \end{cases}$$

From the theory of reproducing kernel Hilbert spaces (RKHS), a vector space V is characterized by the choice of a kernel $K : \mathbb{R}^d \times \mathbb{R}^d \rightarrow \mathbb{R}$, such that, for any $(v, x, \alpha) \in V \times \mathbb{R}^d \times \mathbb{R}^d$, we have:

$$\langle v(x), \alpha \rangle_{\mathbb{R}^d} = \langle v, K(\cdot, x)\alpha \rangle_V. \quad (2)$$

We estimate the vector field v by maximizing the following functional:

$$J(u, v) = \int_{\partial\Omega} \langle v, \epsilon n \rangle d\sigma + \int_{\Omega} \langle v, u \rangle dx - \frac{1}{2} \|v\|_V^2 \quad (3)$$

where u is a unit vector field on Ω and $\|\cdot\|_V$ is the Hilbert norm of $v \in V$, which is an RKHS.

If both u and ϵ are fixed, the problem is quadratic and v can be easily calculated from the formula:

$$v(x) = \int_{\partial\Omega} K(x, y) \epsilon(y) n(y) d\sigma(y) + \int_{\Omega} K(x, y) u(y) dy \quad (4)$$

Proof For any variation δv , we have:

$$\frac{\partial J}{\partial v} \cdot \delta v = \int_{\partial\Omega} \langle \delta v, \epsilon n \rangle + \int_{\Omega} \langle \delta v, u \rangle - \langle v, \delta v \rangle_V = 0 \quad (5)$$

By choosing $\delta v = K(\cdot, x)\alpha$ and using the property expressed by (2) in the last term of (5), we have:

$$\langle v(x), \alpha \rangle = \int_{\partial\Omega} \langle K(\cdot, x)\alpha, \epsilon n \rangle + \int_{\Omega} \langle K(\cdot, x)\alpha, u \rangle \quad (6)$$

By applying the relation in (4) to the functional, we have:

$$\begin{aligned} J(u, v) &= \frac{1}{2} \int_{\Omega} u(y)^T K(x, y) u(x) dx dy \\ &+ \int_{\partial\Omega} \epsilon(y)^T n(y) K(x, y) \epsilon(x) n(x) d\sigma(x) d\sigma(y) \quad (7) \\ &= \frac{1}{2} \|u + \epsilon n\|_V^* \end{aligned}$$

Thus, the variational formulation leads to a problem involving the maximization of a dual norm on vector fields. The smoothness of v is related to the fact that the linear form $u + \epsilon n$ has a large dual norm.

2) *Extension to anisotropic images*: Let Φ be an application that maps a volume Ω in physical space to a volume $\tilde{\Omega} = \Phi(\Omega)$ in the image space. In our case, Φ is a linear transformation of type $\Phi(x, y, z) = (x, y, z/a)$ where a is the anisotropy factor. We define $\Psi = \Phi^{-1}$, and we denote by A the matrix of the application $D\Phi$, and by \tilde{n} the normal at $\partial\tilde{\Omega}$. Also, let K_p be the kernel in physical space and K_i the kernel in image space, such that $K_i(x, y) = K_p(\Phi(x), \Phi(y))$, and V_p and V_i , be, respectively, the RKHS of K_p and K_i .

The vector field \tilde{v} in the image space is given by:

$$\begin{aligned}\tilde{v}(x) &= \int_{\tilde{\Omega}} K_i(x, y) \frac{u(y)}{\det(A)} dy \\ &+ \int_{\partial\tilde{\Omega}} K_i(x, y) \tilde{\epsilon}(y) \frac{A^T \tilde{n}(y)}{\det(A)} d\tilde{\sigma}(y)\end{aligned}\quad (8)$$

Proof $\forall v \in V_p$, we have $v \circ \Psi \in V_i$ and $\|v\|_{V_p} = \|v \circ \Psi\|_{V_i}$. By substitution in the standard variational formulation (3), we have:

$$\begin{aligned}J(u, v) &= \int_{\partial\Omega} \langle v, \epsilon n \rangle d\sigma + \int_{\Omega} \langle v, u \rangle dx - \frac{1}{2} \|v\|_V^2 \\ &= \int_{\partial\tilde{\Omega}} \langle v \circ \psi, \epsilon n \circ \psi \rangle \det(D\Psi) d\tilde{\sigma} \\ &+ \int_{\tilde{\Omega}} \langle v \circ \Psi, u \circ \Psi \rangle \det(D\Psi) dx - \frac{1}{2} \|v \circ \Psi\|_{V_i}^2\end{aligned}\quad (9)$$

Considering that $\partial\Omega$ is defined implicitly as the zero level set of a function F , then, at a point $x \in \partial\Omega$, the normal $n(x)$ is given by $n(x) = \nabla F(x)$. The surface $\partial\tilde{\Omega}$ and the normal $\tilde{n}(\tilde{x})$ at any point $\tilde{x} = \Phi(x) \in \partial\tilde{\Omega}$ are given by $F \circ \Psi$ and $\nabla(F \circ \Psi)(\tilde{x}) = D\Psi(y)^T n(x)$ respectively.

If we set $\tilde{v} = v \circ \Psi$ and $\tilde{u} = u \circ \Psi$, the first and second terms of (9) become:

$$\int_{\partial\tilde{\Omega}} \frac{\langle \tilde{v}, A^T \tilde{\epsilon} \tilde{n} \rangle}{\det(A)} d\tilde{\sigma} \text{ and } \int_{\tilde{\Omega}} \frac{\langle \tilde{v}, \tilde{u} \rangle}{\det(A)} dx.$$

Similarly to (5) in the isotropic case, we can write the following variational formulation:

$$\frac{\partial J}{\partial v} \cdot \delta \tilde{v} = \int_{\partial\tilde{\Omega}} \frac{\langle \delta \tilde{v}, A^T \tilde{\epsilon} \tilde{n} \rangle}{\det(A)} + \int_{\tilde{\Omega}} \frac{\langle \delta \tilde{v}, \tilde{u} \rangle}{\det(A)} - \langle \tilde{v}, \delta \tilde{v} \rangle_{V_i} = 0 \quad (10)$$

Which, for $\delta \tilde{v} = K_i(\cdot, x) \alpha$ leads us to

$$\langle \tilde{v}(x), \alpha \rangle = \int_{\partial\tilde{\Omega}} \frac{\langle K_i(\cdot, x) \alpha, A^T \tilde{\epsilon} \tilde{n} \rangle}{\det(A)} + \int_{\tilde{\Omega}} \frac{\langle K_i(\cdot, x) \alpha, \tilde{u} \rangle}{\det(A)} \quad (11)$$

From this, (8) is deduced.

IV. TEMPLATE ESTIMATION FOR POPULATION ANALYSES

The approaches followed throughout this article to 1) estimate a template from a set of several thickness maps and 2) project those maps onto the template are presented below.

A. Template estimation

We propose to estimate a template central surface based on the approach presented by [7], which is implemented in the freely available software bundle Deformetrica¹. Although various alternative template creation methods exist [8, 9, 10, 11], a thorough review would be out of the scope of this paper. Here, we shall limit ourselves to a brief description of the approach and to justifying its suitability to our problem.

In brief, the approach proceeds as follows. Given a set of N subjects and their respective central surfaces S^1, \dots, S^N , as well as an initial template shape T_0 , the method simultaneously estimates a template shape T and 3D nonlinear diffeomorphic

deformations that map this template to each S^i . All shapes are considered to be embedded in 3D space (ambient space), and each template-to-subject deformation is seen as a particular deformation of the underlying 3D space. Template-to-subject deformations are computed with a sparse parametrization [12] of the Large Deformation Diffeomorphic Metric Mapping (LDDMM) framework [13, 14]. For this, the deformation $\phi^{\alpha_0^i}(T_0)$ from the template to the i -th subject is parametrized by a set of control points c_0 in the ambient space and their set of associated momentum vectors α_0^i . Template estimation then translates into the following optimization criterion:

$$\begin{aligned}E(T_0, c_0, \alpha_0^i) &= \sum_{i=1}^N \frac{1}{2\sigma^2} d_W \left(\phi^{\alpha_0^i}(T_0), S^i \right)^2 \\ &+ \sum_{i=1}^N \|v_0^i\|_V^2\end{aligned}\quad (12)$$

where σ can be interpreted as a Lagrange multiplier and $\|v_0^i\|_V$ is the norm of the initial velocity field v_0^i in a pre-Hilbert space V . This norm represents the length of the geodesic path defined by the diffeomorphic flow of T_0 to S^i . The term $d_W \left(\phi^{\alpha_0^i}(T_0), S^i \right)^2 = \|\phi^{\alpha_0^i}(T_0), S^i\|_W^2$ is the varifold distance [15] between two shapes, which defines the data attachment term.

Thus, this deformation model provides diffeomorphic (smooth and invertible) deformations which are thought to be consistent with plausible anatomical deformations. This is particularly appealing in order to realistically transport hippocampal subregions across subjects. The parameters c_0 and α_0^i define a flow of diffeomorphisms that transform the template into subject i . They are estimated through the minimization of the varifold distance between the deformed template and each S^i . The varifold metric between surfaces presents various advantages. First, like the currents metric [16], it is robust to inconsistencies in the orientation of mesh normals, as well as to mesh imperfections such as holes or spikes, and it does not require to explicitly mark corresponding landmarks. On the other hand, it can deal with folded shapes better than currents [16]. This latter property is specifically attractive since the hippocampal ribbon presents a highly convoluted surface.

B. Projection of thickness maps onto the template

Based on the previous template estimation, the shape variations of the central surfaces can directly be studied through statistical analysis of the deformations that map the template to each individual. However, it would also be desirable to analyze the local thicknesses. This requires the projection of individual thickness maps onto the template central surface.

Consider the central surface as a triangle mesh, composed of a set of faces and vertices, represented by their spatial coordinates in \mathbb{R}^d , as well as a thickness attribute associated to each vertex. Let V_i and $T_i(v_i)$ represent the set of vertices and vertex thickness values of the i -th central surface mesh. Similarly, let V_t and $T_t(v_t)$ be the analogous elements of the template central surface mesh, whereas V_t^i and $T_t^i(v_t^i)$

¹<http://www.deformetrica.org>

represent the same elements for the template central surface mesh transformed according to the registration that maps the template to the i -th subject. Thickness values for $v_{ti} \in V_{ti}$ are computed based on those associated to $v_i \in V_i$ through radial basis function (RBF) interpolation. Among distinct existing RBF functions [17], the one adopted here was introduced by [18] and offers compact support, which ensures locality of the interpolation. This function is defined as:

$$\psi^s(r) = \left(1 - \frac{r}{s}\right)^4 + \left(4\frac{r}{s} + 1\right), \quad (13)$$

where $r = \|v_{ti} - v_i\|$, s is a scale parameter and ψ^s is C^2 on \mathbb{R} .

REFERENCES

- [1] T. R. Henry, M. Chupin, S. Lehericy, J. P. Strupp, M. A. Sikora, Z. Y. Sha *et al.*, “Hippocampal sclerosis in temporal lobe epilepsy: findings at 7T,” *Radiology*, vol. 261, no. 1, p. 199–209, 2011.
- [2] C. Boutet, M. Chupin, S. Lehericy, L. Marrakchi-Kacem, S. Epelbaum, C. Poupon *et al.*, “Detection of volume loss in hippocampal layers in Alzheimer’s disease using 7T MRI: a feasibility study.” *Neuroimage Clin*, vol. 5, pp. 341–348, 2014.
- [3] P. A. Yushkevich, B. B. Avants, J. Pluta, S. Das, D. Minkoff, D. Mechanic-Hamilton *et al.*, “A high-resolution computational atlas of the human hippocampus from postmortem magnetic resonance imaging at 9.4 T.” *Neuroimage*, vol. 44, no. 2, pp. 385–398, Jan 2009.
- [4] L. Marrakchi-Kacem, A. Vignaud, J. Sein, J. Germain, T. R. Henry, C. Poupon *et al.*, “Robust imaging of hippocampal inner structure at 7T: in vivo acquisition protocol and methodological choices,” *Magnetic Resonance Materials in Physics, Biology and Medicine*, vol. 29, no. 3, pp. 475–489, 2016.
- [5] H. Duvernoy, *The Human Hippocampus: Functional Anatomy, Vascularization and Serial Sections with MRI*. Springer, 2005.
- [6] R. Insausti and D. G. Amaral, “Hippocampal formation,” in *The Human Nervous System: Second Edition*. Elsevier Inc., 2003.
- [7] S. Durrleman, M. Prastawa, N. Charon, J. R. Korenberg, S. Joshi, G. Gerig *et al.*, “Morphometry of anatomical shape complexes with dense deformations and sparse parameters.” *Neuroimage*, vol. 101, pp. 35–49, Nov 2014.
- [8] S. Joshi, B. Davis, M. Jomier, and G. Gerig, “Unbiased diffeomorphic atlas construction for computational anatomy.” *NeuroImage*, vol. 23 Suppl 1, pp. S151–S160, 2004.
- [9] P. T. Fletcher, S. Venkatasubramanian, and S. Joshi, “The geometric median on riemannian manifolds with application to robust atlas estimation.” *Neuroimage*, vol. 45, no. 1 Suppl, pp. S143–S152, Mar 2009.
- [10] T. Chen, A. Rangarajan, S. J. Eisenschenk, and B. C. Vemuri, “Construction of a neuroanatomical shape complex atlas from 3D MRI brain structures.” *Neuroimage*, vol. 60, no. 3, pp. 1778–1787, Apr 2012.
- [11] S. Zhang, Y. Zhan, X. Cui, M. Gao, J. Huang, and D. Metaxas, “3D anatomical shape atlas construction using mesh quality preserved deformable models,” *Computer Vision and Image Understanding*, vol. 117, no. 9, pp. 1061 – 1071, 2013.
- [12] S. Durrleman, S. Allasonnière, and S. C. Joshi, “Sparse adaptive parameterization of variability in image ensembles,” *Int J Comp Vision*, vol. 101, no. 1, pp. 161–183, 2013.
- [13] S. Joshi and M. Miller, “Landmark matching via large deformation diffeomorphisms,” *Image Processing, IEEE Transactions on*, vol. 9, no. 8, pp. 1357–1370, Aug 2000.
- [14] M. F. Beg, M. I. Miller, A. Trouné, and L. Younes, “Computing large deformation metric mappings via geodesic flows of diffeomorphisms,” *International Journal of Computer Vision*, vol. 61, no. 2, pp. 139–157, 2005.
- [15] N. Charon and A. Trouné, “The varifold representation of nonoriented shapes for diffeomorphic registration,” *siam J. Imaging Sciences*, vol. 6, no. 4, pp. 2547–2580, 2013.
- [16] M. Vaillant and J. Glaunès, “Surface matching via currents.” *Inf Process Med Imaging*, vol. 19, pp. 381–392, 2005.
- [17] M. D. Buhmann, *Radial Basis Functions*. New York, NY, USA: Cambridge University Press, 2003.
- [18] H. Wendland, “Piecewise polynomial, positive definite and compactly supported radial functions of minimal degree,” *Advances in Computational Mathematics*, vol. 4, no. 1, pp. 389–396, 1995.